A GPU-Accelerated Modified Unsharp-Masking Method for High-Frequency Background-Noise Suppression

BHASKAR JYOTI BORAH[1,2] **AND CHI-KUANG SUN**[1,2,3,4,5,6], **(Fellow, IEEE)**

[1]Department of Electrical Engineering, National Taiwan University, Taipei 10617, Taiwan
[2]Graduate Institute of Photonics and Optoelectronics, National Taiwan University, Taipei 10617, Taiwan
[3]Graduate Institute of Biomedical Electronics and Bioinformatics, National Taiwan University, Taipei 10617, Taiwan
[4]Institute of Medical Device and Imaging, National Taiwan University, Taipei 10051, Taiwan
[5]Molecular Imaging Center, National Taiwan University, Taipei 10617, Taiwan
[6]Research Center for Applied Sciences, Academia Sinica, Taipei 11529, Taiwan

Corresponding author: Chi-Kuang Sun (sun@ntu.edu.tw)

ABSTRACT A digitized analog signal often encounters a high-frequency noisy background which degrades the signal-to-noise ratio (SNR) particularly in case of low signal strength. Despite quite a lot of hardware- and software-based approaches have been reported to date to deal with the noise issue, it is still a challenging task to real-time retrieve the noise-contaminated low-frequency information efficiently without degrading the original bandwidth. In this paper, we report a modified unsharp-masking (UM)-based Graphics Processing Unit (GPU)-accelerated algorithm to efficiently suppress a high-frequency noisy background in a digitized two-dimensional image. The proposed idea works effectively even if noise-density is high and signal of interest is comparable or weaker than the maximum noise level. While suppressing the noisy background, the original resolution remains least compromised. We first explore the effectiveness of the algorithm by means of simulated images and subsequently extend our demonstration towards a real-world life-science imaging application. Securing a potential for real-time applicability, we implement the algorithm via Compute Unified Device Architecture (CUDA)-acceleration and preserve a <300 μs processing time for a 1000×1000-sized 8-bit data set.

INDEX TERMS High-frequency noise cancellation, unsharp-masking, life-science imaging, CUDA-acceleration.

I. INTRODUCTION

In the process of digitization of an analog signal, due to various instrumental and environmental factors, the digitized data set might get contaminated with high-frequency noises. Quite a lot of analog filters [1]–[4] are available to improve the signal quality, which however require dedicated hardware configuration and might limit the effective bandwidth of an acquisition system.

On the other hand, post-acquisition digital signal processing is a promising idea to deal with this issue without a need of additional electronic circuitry. In case the signal of interest is strong enough, a global threshold can be applied to reject the weak noisy background while passing the strong signal as it is. One can effectively suppress weak and/or

low-density noises by means of various low-pass filters, for instance, gaussian blur [5], mean filter [6], bilateral filter [7], median filter [8], wavelet threshold [9], wiener filter [10], etc. A few methods were reported involving subtraction of a low-pass-filtered input. An interesting report [11] computed a median-filtered low-passed image and subtracted from input image to minimize the background. However, such a blurred version usually holds a weaker intensity compared to the original one, and also contains the low-frequency structures in it. Therefore, the noises do not reduce down to the zero level, and the signal of interest experiences a reduction in intensity and a possible loss of dynamic range which might tend to worsen if the blurred version is amplified prior to subtraction. Likewise, another report [12] obtained a smooth illumination gradient surface by means of mean filtering and subtracted from the original one to suppress the background. Another report [13] utilized a top-hat based algorithm to improve

the issue of non-uniform background illumination. Another approach [14] for dark-area-suppression involved a regional-maxima method which finds the brightest pixels in discrete areas and subsequently separates them out from the dark pixels, however, this method alters the absolute intensity values. A deep learning-based study [15] introduced a neural network with a U-net-type architecture for eliminating arbitrarily structured background in an image of a point source, of course requiring a training process accordingly. Another noteworthy approach is rolling-ball background subtraction [16]. In this method local average is calculated around a pixel covering a pre-defined circular area, and subsequently this averaged value is subtracted to suppress the background. This method however introduces artifacts when a larger ball-radius is used.

Aside from the above methods, unsharp-masking (UM) [17] is another widely used image-processing technique traditionally used for image-sharpening. A scaled mask is usually added to the input image, where the mask is obtained by either subtracting a blurred version of the input from the input itself, or directly applying a high pass filter to the input. The mask usually consists of edge-information which when added to the input, helps to sharpen the structures. This algorithm however does not reduce the background noise. In fact, the mask often contains high-frequency noise components along with edge-information, and thus can lead to noise-amplification. Over the past several years, quite a few UM-inspired techniques [18]–[31] were reported which have significantly improved the image quality and a few of them further dealt with the noise amplification issue as well.

Nevertheless, the existing techniques might not produce satisfactory results especially when noise density is high, signal of interest is comparable or even weaker than maximum noise level, and bandwidth-preservation as well as a high enough processing speed become primary concerns. In this paper, we demonstrate a modified UM-based algorithm which unlike a traditional UM, suppresses high-frequency noises in a background while leaving the original resolution least compromised. We demonstrate the algorithm in case of both simulated and life-science imaging examples to validate its robustness and wide-range of applicability. Remarkably, the algorithm is implemented utilizing NVIDIA's CUDA-acceleration in order to maintain a high processing speed of $<300\ \mu s$ for a 1000×1000-sized 8-bit data set, justifying its potential to be applied in real-time applications.

II. RESULTS

A. MATHEMATICAL FORMULATION OF THE PROPOSED ALGORITHM

Conventionally, an UM algorithm can be expressed as

$$\mathrm{F}\,(r, c) = f\,(r, c) + \alpha \times (f\,(r, c) - \mathrm{G}_{\mathrm{M \times M}} \otimes f\,(r, c)) \quad (1)$$

where, $f\,(r, c)$ and $\mathrm{F}\,(r, c)$ are the input and output data sets, respectively; $\mathrm{G}_{\mathrm{M \times M}}$ is a gaussian blur kernel with $\mathrm{M \times M}$ size; and α is a multiplicative factor. In such an approach, first an unsharp (blurred) version of the input is subtracted from the

input which provides a mask consisting of the high-frequency components. A multiplicative factor α is used to control the strength of this mask and subsequently the mask is added to the original input to boost the high-frequency components.

We now demonstrate a modified UM algorithm, which is dedicated to suppress high-frequency noises in a background while mostly preserving useful information. Let us assume $f\,(r, c)$ and $\mathrm{F}\,(r, c)$ are the input and output data sets, respectively, with a size of R × C. The modified method can be mathematically expressed as

$$\mathrm{F}\,(r, c) = f\,(r, c) - \beta$$
$$\times \left[\mathrm{G}_{\mathrm{M \times M}} \otimes \left(L^{U}\,(r, c) - g\,(r, c) \right) \right]; \quad (2)$$

and,

$$g\,(r, c) = \alpha \times f\,(r, c), \quad (3)$$

$$g\,(r, c) \xrightarrow[\substack{3 \times downscaling \\ R \times C \to \mathrm{R}^{/} \times \mathrm{C}^{/}}]{} g^{D}\,(r^{/}, c^{/}), \quad (4)$$

$$L\,(r^{/}, c^{/}) = \mathrm{G}_{29 \times 29} \otimes g^{D}\,(r^{/}, c^{/}), \quad (5)$$

$$L\,(r^{/}, c^{/}) \xrightarrow[\substack{Upscaling \\ \mathrm{R}^{/} \times \mathrm{C}^{/} \to R \times C}]{} L^{U}\,(r, c); \quad (6)$$

where, α and β are two amplification factors, $\mathrm{G}_{29 \times 29}$ and $\mathrm{G}_{\mathrm{M \times M}}$ are two gaussian blur kernels with kernel sizes of 29×29 and M × M, respectively, $\otimes$ denotes a convolution operation, r, c denote the vertical- and horizontal-axis data points, respectively in the R × C-sized data sets, and $r^{/}, c^{/}$ denote the same for the $\mathrm{R}^{/} \times \mathrm{C}^{/}$-sized data sets. Fig. 1A depicts the working principle of the algorithm with a simplified block diagram. The input data $f\,(r, c)$ with R×C samples (marked as INPUT in Fig. 1A) is amplified by multiplying with a suitable factor α, where $1.0 < \alpha \le 5.0$. Its purpose is to boost the weak low-frequency information preferably close to saturation. The result $g\,(r, c)$ in Equation (3) is denoted as AMP1 in Fig. 1A. The next step is to obtain a smooth layer of AMP1. A $3 \times$ downscaling is first performed preferably by means of pixel-binning (RESIZE1 in Fig. 1A and $g^{D}\,(r^{/}, c^{/})$ in Equation (4)), and a 29×29-kernel gaussian blur is applied to $g^{D}\,(r^{/}, c^{/})$. The result $L\,(r^{/}, c^{/})$ in Equation (5) with $\mathrm{R}^{/} \times \mathrm{C}^{/}$ samples is denoted as BLUR1 in Fig. 1A. By means of a bilinear interpolation, $L\,(r^{/}, c^{/})$ is upscaled to original size of R × C. The result is represented as $L^{U}\,(r, c)$ in Equation (6) and RESIZE2 in Fig. 1A. Now, $g\,(r, c)$ is subtracted from $L^{U}\,(r, c)$ (Fig. 1A, SUB1) with a purpose of yielding zero intensities to the noisy samples as well as the locations of low-frequency structures, while leaving non-zero intensities to the neighbors of the noisy samples. In order to re-distribute the non-zero intensities, this subtraction result is again convolved with an M × M-sized gaussian kernel (M ≤ 7), represented as $\mathrm{G}_{\mathrm{M \times M}} \otimes \left(L^{U}\,(r, c) - g\,(r, c) \right)$ in Equation (2) and BLUR2 in Fig. 1A. Subsequently, BLUR2 is boosted by a multiplicative factor of β, where $1.0 < \beta \le 10.0$, and a subtraction-mask is generated as $\beta \times \left[\mathrm{G}_{\mathrm{M \times M}} \otimes \left(L^{U}\,(r, c) - g\,(r, c) \right) \right]$ in Equation (2), and AMP2 or MASK in Fig. 1A. Finally, the MASK is subtracted
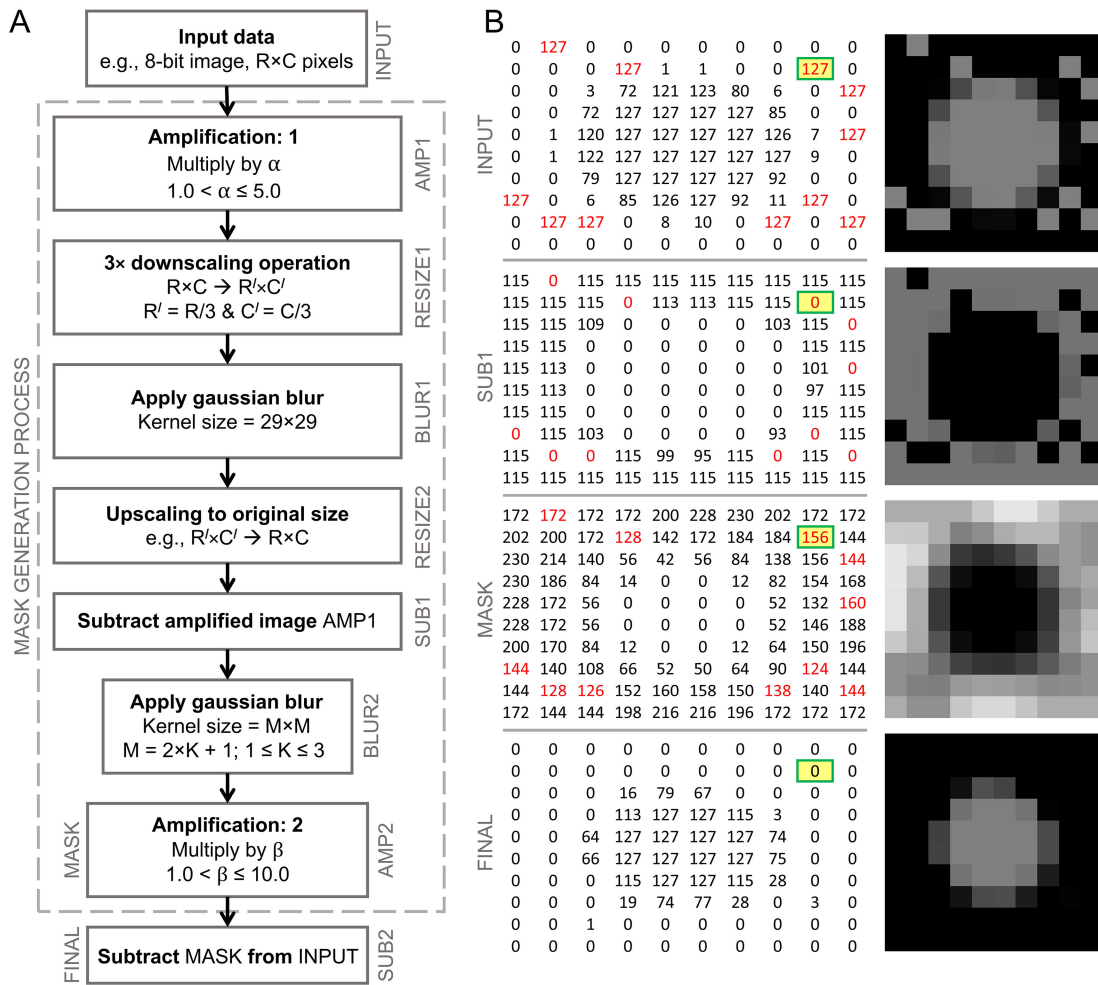
FIGURE 1. Working principle of the algorithm. (A) Block diagram representation, where, INPUT is a noise-affected data set, AMP1 is α-times amplification of INPUT, RESIZE1 is 3$\times$ downscaled AMP1, BLUR1 is 29$\times$29-kernel gaussian blurred RESIZE1, RESIZE2 is upscaled version of BLUR1, SUB1 is subtraction of AMP1 from RESIZE2, BLUR2 is M$\times$M-kernel gaussian blurred SUB1, MASK or AMP2 is β-times amplification of BLUR2, and FINAL or SUB2 is subtraction of MASK from INPUT, (B) pixel-level illustration of the crucial intermediate steps with a small 10$\times$10-sized 8-bit grayscale input image, where INPUT, SUB1, MASK, and FINAL follow the same notations as in (A). The yellow-marked noise pixel in INPUT is reduced down to zero in FINAL, while preserving the low-frequency information contents.

from the INPUT, i.e., $f(r, c)$ to produce the final result $F(r, c)$ as represented by Equation (2) and SUB2 or FINAL in Fig. 1A.

Fig. 1B provides a pixel-level illustration of the crucial intermediate steps with a small 10×10-sized 8-bit grayscale image as INPUT. With $\alpha = 2.0$, AMP1 is obtained. A 3$\times$ downscaling is performed to produce 3×3-pixeled RESIZE1. Subsequently, a 29×29-kernel gaussian blur is applied to produce a uniform layer BLUR1 with intensity of 115 in this case, which is interpolated to 10×10 pixels as RESIZE2. In this example, INPUT size is much smaller than blur-kernel size. Therefore, all pixels in BLUR1 and RESIZE2 attain a value of 115. For a larger INPUT size, RESIZE2 is essentially a smooth layer of the AMP1. Now, SUB1 is obtained by subtracting AMP1 from RESIZE2. Let us consider a high-frequency-noise pixel in INPUT (Fig. 1B), $f(9, 2) = 127$, i.e., the yellow-marked pixel surrounded mostly by darker

pixels. In SUB1 (Fig. 1B), this noise pixel has become zero, i.e., $f_{SUB1}(9, 2) = 0$, while its neighbors attain non-zero values, for instance $f_{SUB1}(9, 1) = 115$. Additionally, the low-frequency structure in the central-region is now filled with zeros. Note that each negative subtraction result is replaced with a zero. A 3×3-kernel gaussian blur (M = 3) is applied to SUB1 to redistribute the non-zero intensities with the purpose of making $f_{SUB1}(9, 2)$ non-zero which is essentially the noise location. The resultant image BLUR2 is multiplied by $\beta = 2.0$ to strengthen the non-zero values so as to obtain a layer of strong enough pixels corresponding to the noisy-background regions. This β-amplified image is depicted as MASK in Fig. 1B, where $f_{MASK}(9, 2)$ has now attained a value of 156 which is indeed higher than $f(9, 2)$. Finally, after subtraction of MASK from the INPUT, $f_{FINAL}(9, 2)$ is reduced down to zero, while preserving the low-frequency structure at the center.
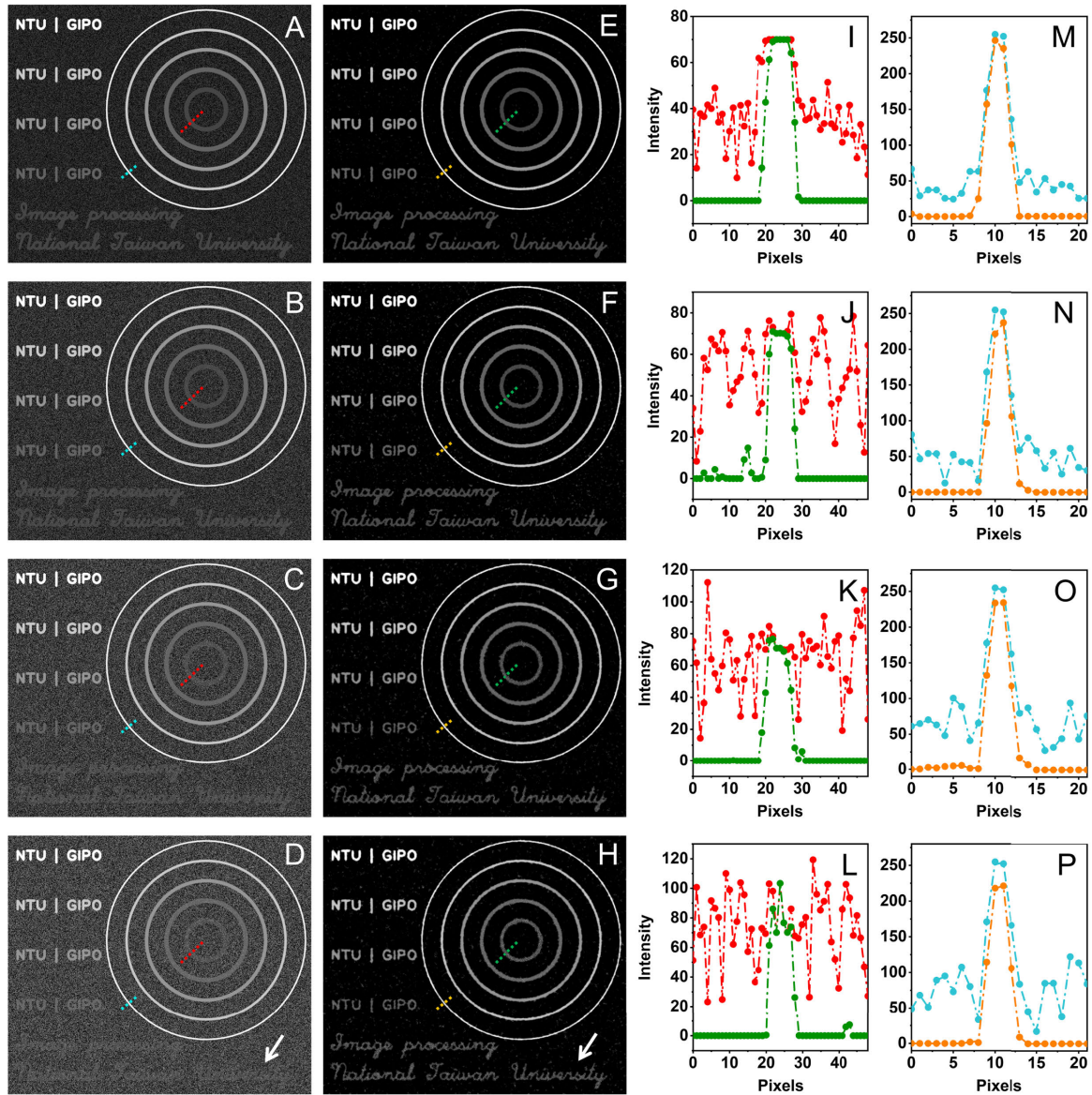
FIGURE 2. Demonstration of background-noise suppressing ability of the algorithm with simulated 8-bit grayscale image. (A)-(D) Noise-affected INPUTs added with random numbers in the ranges of (A) 0-75, (B) 0-100, (C) 0-125, and (D) 0-140, respectively, (E)-(H) background-noise-suppressed images corresponding to (A)-(D), respectively, where $\alpha = 3.6$ in each case, and β & M are varied as (E) $\beta = 3.0$, M = 5, (F) $\beta = 3.5$, M = 5, (G) $\beta = 4.0$, M = 7, and (H) $\beta = 5.0$, M = 7, (I)-(L) red & green curves in each case represent intensity profiles along the red & green-dashed lines in the respective noise-affected (A)-(D) & noise-suppressed (E)-(H) images. Weak-intensity circle at the center was recovered in each case. Barely visible white-arrow-marked texts in (D) become recognizable in (H) after noise-suppression. (M)-(P) Intensity profiles along the cyan & orange-dashed lines in the respective noise-affected (A)-(D) and noise-suppressed (E)-(H) images. In each case, resolution remains least compromised.

B. EFFECT OF THE CONTROL PARAMETERS

The effectiveness of the proposed algorithm can be controlled with 3 parameters in Equation (2). First one is the pre-amplification factor α, which helps to boost the weak-intensity information preferably close to saturation. Ideally, α can be chosen as inverse of minimum intensity of interest multiplied by 255.0 (for an 8-bit data set). The second parameter is M, i.e., the kernel size of the second gaussian blur. M must be an odd number greater than 1, yet should be kept as low as possible. For higher noise contamination however, a higher value of M will be helpful. The third parameter is the post-amplification factor β. Depending on the noise contamination level, higher value of β should be employed. Recommended ranges for α, M, and β are $1.0 < \alpha \leq 5.0$, $3 \leq M \leq 7$, and $1.0 < \beta \leq 10.0$, respectively. Decimal points indicate that floating point numbers are applicable.

C. DEMONSTRATION OF THE ALGORITHM VIA SIMULATED GRAYSCALE IMAGE

To demonstrate the effectiveness of the algorithm we present an example with a 610×520-pixeled 8-bit grayscale image in Fig. 2. Starting from the top-left corner of the image,

we add 4 lines of regular texts with varying intensities of 255, 200, 150, and 100, respectively. At the bottom-most part, we add two lines of hand-writing-font texts, both at an intensity of 70. On the right side, multiple circles are drawn with similarly varying intensities of 70, 100, 150, 200, and 255 from the innermost to the outermost circle, sequentially. Now, noise-affected images in Figs. 2A-D are obtained by adding random numbers in the ranges of 0-75, 0-100, 0-125, and 0-140, respectively. Figs. 2E-H depict the background-noise-suppressed results corresponding to Figs. 2A-D, respectively; where, $\alpha = 3.6$ is set for all the cases (as the known minimum intensity of interest is 70.0 for the 8-bit input images), and the remaining two parameters are respectively varied as (E) $\beta = 3.0$, M = 5, (F) $\beta = 3.5$, M = 5, (G) $\beta = 4.0$, M = 7, and (H) $\beta = 5.0$, M = 7. Consider the plots depicted in Figs. 2I-L, where the red and green curves in each case represent the intensity profiles along the red and green-dashed lines in the respective noise-affected (Figs. 2A-D) and noise-suppressed (Figs. 2E-H) images. In each case, the weakest circle with an intensity of 70 is recovered. It is remarkable that, Fig. 2D was contaminated with a maximum noise level of up-to 140, which is twice this signal intensity. Nevertheless, the algorithm successfully retrieves the weak signal structures while suppressing the nearby higher-intensity high-frequency noises. Additionally, an observation to the white-arrow-marked hand-writing-font texts in Figs. 2D and H justifies the effectiveness of the algorithm. In Fig. 2D, these texts with an intensity of 70 are barely visible, whereas, after noise-rejection, the texts become well-recognized in Fig. 2H. An advantage of our approach is that the output image is obtained with a mask-subtraction only, and does not involve a blurring operation. Therefore, the algorithm does not worsen the image resolution. The cyan and orange curves in Figs. 2M-P represent the intensity profiles along the cyan and orange-dashed lines in the respective noise-affected (Figs. 2A-D) and noise-suppressed (Figs. 2E-H) images. In each case, the resolution was observed to be least compromised.

D. FEASIBILITY OF THE ALGORITHM TO BE APPLIED IN A COLOR IMAGE

Extending our demonstration to a color image, we prepare another 475×375-pixeled 24-bit BGR-image, where the three 8-bit channels are indicated by B, G, and R, standing for blue, green and red colors, respectively. For our analysis, smoothly varying colored texts are drawn with a maximum allowed intensity of 128 for each individual channel. For each channel, independent set of random numbers is added in the ranges of 0-100, 0-150, 0-200, and 0-255, and the noise contaminated BGR-images thus obtained are depicted in Figs. 3A-D, respectively (marked as *Input* in each case). For applying our algorithm, we first split the BGR-input into blue, green, and red channels which are shown as B_{IN}, G_{IN}, and R_{IN}, respectively. The individual channels in each case in Figs. 3A-D are used as INPUTs and are noise-suppressed by means

of the proposed algorithm with $\alpha = 2.0$, and (A) $\beta = 7.0$, M = 5, (B) $\beta = 8.0$, M = 5, (C) $\beta = 8.0$, M = 7, and (D) $\beta = 9.0$, M = 7, respectively. The output noise suppressed channels are depicted as B_{OUT}, G_{OUT}, and R_{OUT}, which are merged together to form the noise-suppressed BGR-image marked as *Output* in each case (Figs. 3A-D). The plots in Figs. 3E-H correspond to the cases in Figs. 3A-D, respectively, where, red and blue curves in each case depict the intensity profiles along the yellow-dashed lines in the *input* and *output*-BGR images, respectively. Note that, each intensity value in each plot is an average of blue, green, and red intensities. With an observation to the *input* and *output* BGR-images and the corresponding intensity profiles, it is evident that the algorithm has a potential to be applied in a color image. However, it is observed that, with an excessive noise level in each channel, the non-primary color-information might not get recovered effectively.

In Figs. 3A-D, we apply a same level of noise to all the 3 channels in each case, for instance, a noise-level of 0-255 is applied to each channel in Fig. 3D. Therefore, in this example, we utilize the same set of β and M parameters for each channel in a BGR-image. If each channel is contaminated with different noise-levels, choosing different set of parameters might be helpful. Additionally, choice of an optimum α-value is critical for a BGR-image, since the minimum intensity of interest in a channel might go very low while representing certain non-primary colors. Therefore, instead of using a global α, an independent layer of α-values for each channel can be chosen based on the available signal level, which will help to better preserve the structural as well as color information. Note that each BGR-image in Figs. 3A-D consists of 475×375 pixels, and it can be extended up-to any practical size supported by an image-processing library/software. For different sized images, the relevant changing parameter will be the processing speed, which we discuss in the following section II.H.

E. APPLICATION OF THE ALGORITHM IN LIFE SCIENCE IMAGING

Extending our demonstration to a life-science imaging application, we consider a two-photon fluorescence microscopy [32], [33] image as an INPUT being depicted in Fig. 4A with a poor signal to noise ratio (SNR) of less than 5. A dorsal root ganglion sample from a Nav1.8-tdTomato positive mouse was used as sample (see supplemental material). The scanned image with a field of view of $\sim 140 \times 140 \mu m^2$ (770×770 pixels) consists of multiple fine fibers which are mostly contaminated with high-frequency noises at the background. Following the same notations as in previous figures, Fig. 4B shows the AMP1 with $\alpha = 2.0$. Figs. 4C and D show the $3\times$ downscaled and 29×29-kernel gaussian blurred outputs, i.e., RESIZE1 and BLUR1, respectively. Upscaled version of BLUR1, i.e., RESIZE2 is depicted in Fig. 4E. Subtraction result of RESIZE2 and AMP1, i.e., SUB1 is represented in Fig. 4F. With M = 7, Fig. 4G shows BLUR2, i.e., the 7×7-kernel
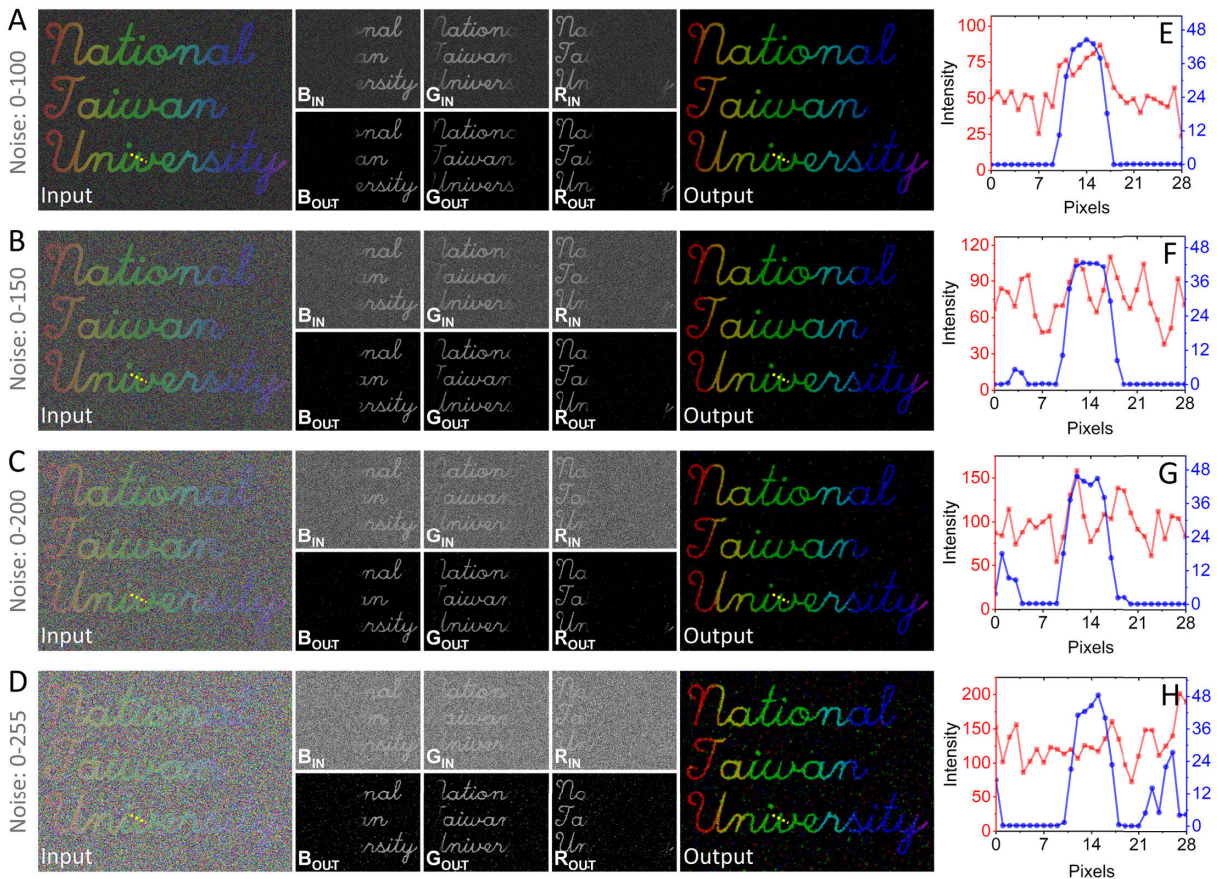
FIGURE 3. Assessing the algorithm with 24-bit BGR-input image. (A)-(D) Noise-affected color images added with random numbers in the ranges of (A) 0-100, (B) 0-150, (C) 0-200, and (D) 0-255, respectively. B_{IN}, G_{IN} & R_{IN} in each case denote blue, green & red-channel inputs, and B_{OUT}, G_{OUT} & R_{OUT} similarly denote the corresponding noise-suppressed outputs obtained with $\alpha = 2.0$, and (A) $\beta = 7.0$, M = 5, (B) $\beta = 8.0$, M = 5, (C) $\beta = 8.0$, M = 7, and (D) $\beta = 9.0$, M = 7, respectively. B_{OUT}, G_{OUT} & R_{OUT} are merged to form the BGR-output in each case. (E)-(H) red & blue curves in each case represent intensity profiles along the yellow-dashed lines in the corresponding noise-affected-input & noise-suppressed-output BGR-images, respectively.

gaussian blurred version of SUB1. With $\beta = 5.0$, the amplified version of BLUR2, i.e., the final MASK is depicted in Fig. 4H. Subsequently, MASK is subtracted from INPUT, and the noise-suppressed image is presented in Fig. 4I, with an SNR of more than 40. Thus, the proposed algorithm successfully suppressed the high-frequency background noises to bring the signal of interest into attention.

F. EFFECT OF α AND β OVER SIGNAL-TO-NOISE RATIO (SNR)

To assess the effect of α and β over the performance of the algorithm, we consider the low-SNR two-photon fluorescence microscopy image (in Fig. 4A) as input, and the value of M is fixed at 7. Now, the value of α is gradually increased as 1.2, 1.6, 2.0, 2.4, and 2.8. For each value of α, the value of β is again varied as 3.0, 4.0, 5.0, 6.0, and 7.0. In this way, the output images are obtained for all the 25 different cases, and are depicted in Fig. 5. For all 25 images, a common 5×5-sized region-of-interest (ROI)-1 is selected corresponding to a moderate intensity structure. Likewise, another common 5×5-sized ROI-2 is selected from a nearby location containing high-frequency noises. Subsequently, for each of

the 25 cases, the mean of signal intensities (μ_{ROI-1}) is calculated for ROI-1, and the standard deviation of noises (σ_{ROI-2}) is calculated for ROI-2. The SNR value is finally obtained as the ratio of μ_{ROI-1} and σ_{ROI-2} in each case. It is observed that, for a fixed reasonable value of α, SNR tends to increase with increase in value of β, and vice versa. When both α and β values are increased, a drastic improvement in SNR is observed. For instance, with $\alpha = 1.2$, $\beta = 3.0$, SNR is 4.72; with $\alpha = 1.6$, $\beta = 4.0$, SNR improves to 8.55; with $\alpha = 2.0$, $\beta = 5.0$, SNR significantly improves to 45.09. However, note that, excessive values of α and β can lead to loss of information, particularly the weaker and finer structures.

G. COMPARISON WITH A FEW ALTERNATIVE APPROACHES

In a simple scenario when: noise density is low, signal strength is comparable or higher than the noise contamination level, and signal of interest is not much corrupted, a high-pass filter can be directly applied to separate out the noises and subsequently can be subtracted from the original input to recover the signal. However, when density and strength of noise are much higher, such an approach might not be
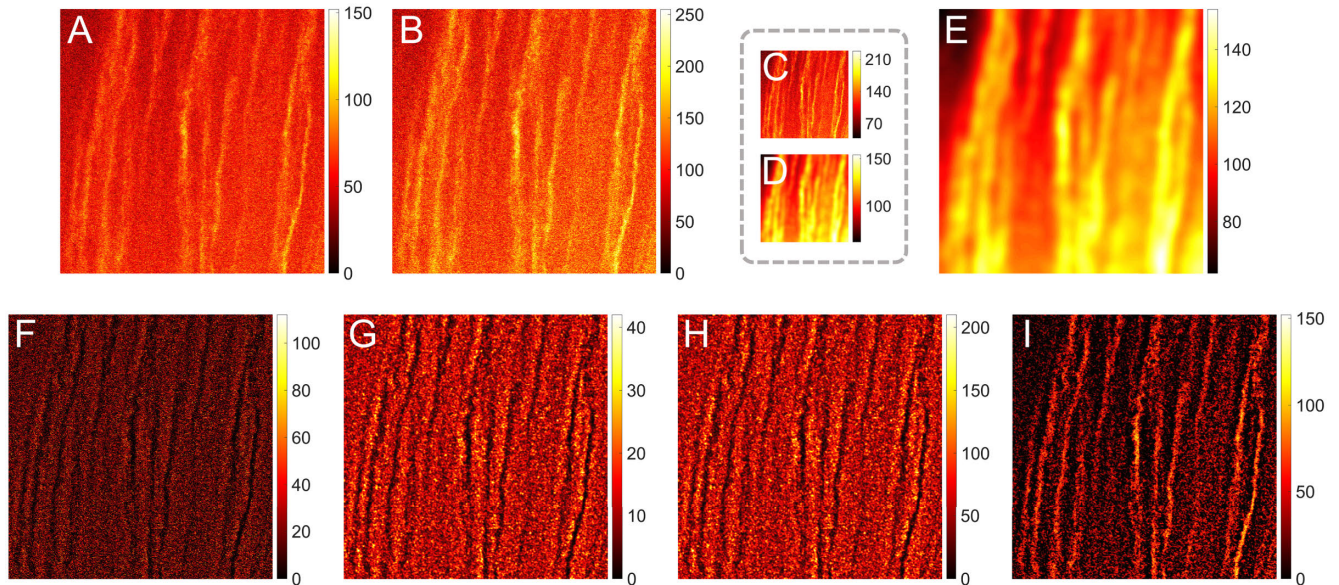
FIGURE 4. Demonstration of background-noise suppressing ability of the algorithm in a life-science imaging application. (A) A low signal-to-noise ratio (SNR < 5) two-photon fluorescence image with a field of view of ~140 × 140 μm^2, (B)-(H) intermediate steps depicting (B) AMP1 with α = 2.0, (C) RESIZE1 with 3× downscaling, (D) BLUR1 with 29 × 29-sized gaussian kernel, (E) RESIZE2 with interpolated upscaling, (F) SUB1, (G) BLUR2 with M = 7, and (H) MASK with β = 5.0, respectively, (I) background-suppressed image with SNR over 40.

able to distinguish the noise-corrupted low-frequency information particularly when signal strength is relatively weaker. For instance, consider the 3 input images in Figs. 6A-C. A Laplacian high-pass filter is applied and a layer/mask with high-frequency components (and edges as well) is generated in each case (Figs. 6D-F). After subtraction of this layer from the input, the resultant image in each case is depicted in Figs. 6G-I, respectively. In the simplest case in Fig. 6A, this idea successfully eliminates the noisy pixels. However, the same idea does not provide satisfactory outcomes for Figs. 6B and C, where noise contaminations are much higher. On the other hand, Figs. 6J-L depict the results of our proposed algorithm for the same inputs in Figs. 6A-C, respectively. We observe that our proposed method efficiently suppressed the noises in each case.

Aside from direct subtraction of a high-passed layer, morphological filtering [34] is another state-of-the-art technique to reduce the noise-issue. Morphological erosion and morphological opening are two promising candidates in this regard. Fig. 7A shows the noise-contaminated image with a noise level of 0-140, the same one obtained in Fig. 2D. Fig. 7B depicts the noise-suppressed result via our proposed algorithm. The results of morphological erosion and opening operations with a 2-pixel-radius circular structure element are depicted in Figs. 7C and D, respectively. In case of erosion, background noises are effectively removed. However, such an operation leads to significant loss of structural information, and thus might result in irreversible resolution loss. In case of opening, a dilation operation is subsequently performed after an erosion, so that the reduced structural details can be compensated. However, in this process, a loss of resolution during erosion might not be possible to recover. The red,

green, blue, and gray curves in Fig. 7J plot the intensity profiles along the white dashed lines in Figs. 7A-D, respectively. It is clearly observed that our algorithm's result (green curve) outperforms both erosion (blue curve) and opening (gray curve) operations, in terms of preserving the original structural and intensity information. Further extending our comparison, utilizing the same noisy input in Fig. 7A, Figs. 7E-I show the results of (E) non-local mean denoising [35], (F-G) rolling ball and sliding paraboloid background subtractions [16], [36], (H) traditional UM [17], and (I) Otsu thresholding [37], respectively (see supplemental material). In Fig. 7K, we plot all the intensity profiles along the yellow-dashed lines in Figs. 7A-B, E-H. It is evident that our algorithm's result (green curve) outperforms the counterparts. Further extending our comparison, we perform an SNR analysis (following the same method used in Fig. 5) for all the images in Figs. 7A-I, and the SNR values are plotted in Fig. 7L. The input image in Fig. 7A holds an SNR of 3.84. After applying the proposed method, it has been improved to 54.5. We observe that morphological erosion and opening results hold SNRs over 13 and 26, respectively, however, with their limitations as we have stated before.

H. ASSESSMENT OF PROCESSING SPEED
To assess the processing speed, we run the algorithm on an i7 9800X CPU, and two CUDA-enabled GPUs, Quadro P1000 and Quadro RTX 8000 with CUDA-core numbers of 640 and 4608, respectively. In Fig. 8A, red, blue, and green curves represent processing time with respect to input image size plotted for 9800X, P1000, and RTX 8000, respectively. For a small image size, processing time is identical for each case. We however observe that, as image size gets
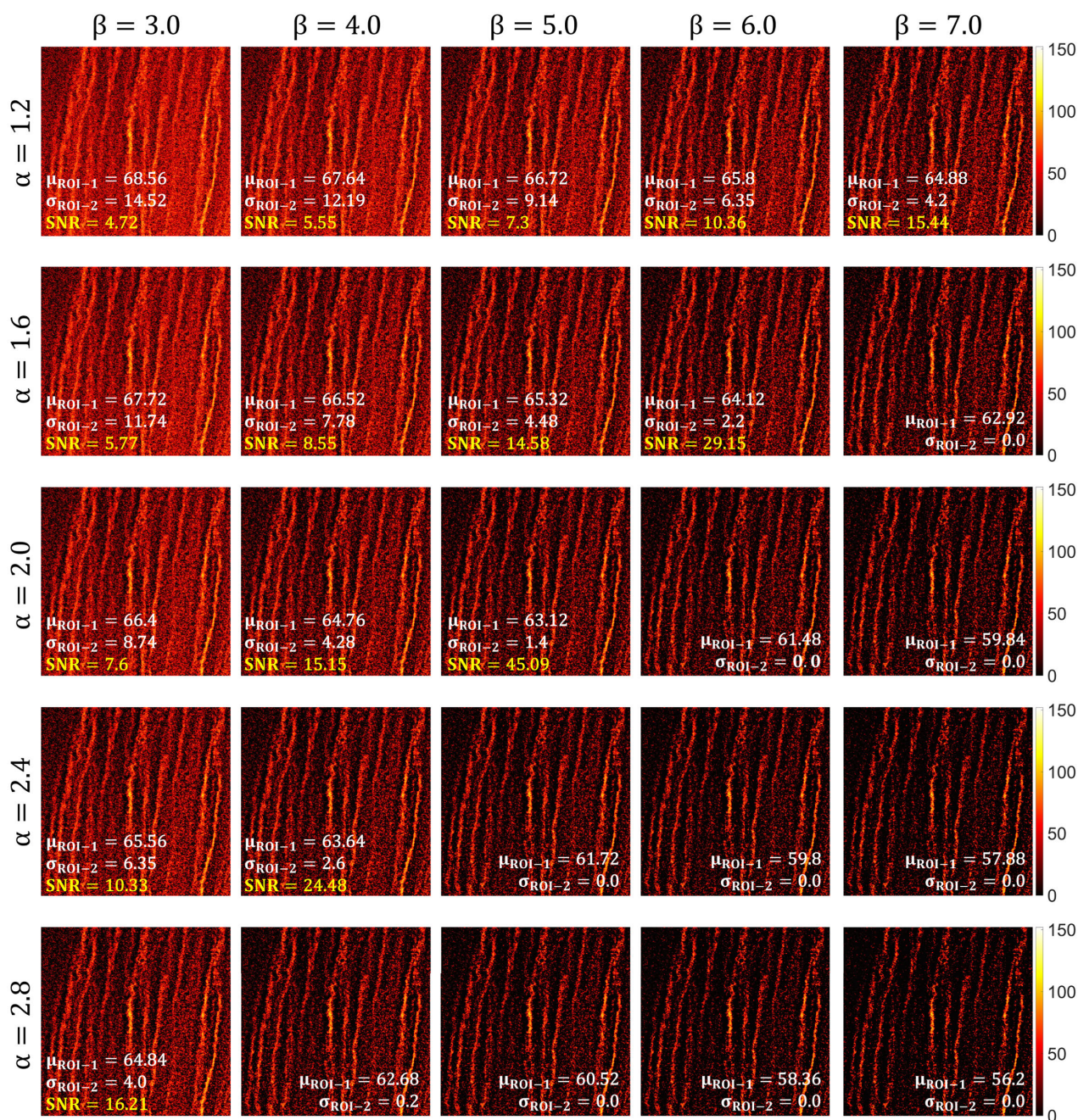
FIGURE 5. Effect of α & β on SNR. A low-SNR (<5) two-photon fluorescence microscopy image is used as INPUT. For M = 7, α is varied as 1.2, 1.6, 2.0, 2.4 & 2.8, and for each α-value, β is varied as 3.0, 4.0, 5.0, 6.0 & 7.0. For a fixed reasonable α-value, SNR tends to increase as β increases, and vice versa. SNR improves rapidly when both α & β-values are increased. For instance, with $\alpha = 1.2$, $\beta = 3.0$, SNR is 4.72; with $\alpha = 1.6$, $\beta = 4.0$, SNR improves to 8.55; with $\alpha = 2.0$, $\beta = 5.0$, SNR significantly improves to 45.09.

larger, CPU-processing time tends to increase exponentially as depicted by the red curve. The blue curve for P1000 indicates an improvement over CPU performance. Eventually, RTX 8000 significantly reduces the processing time as indicated by the flat enough green curve. At 10000×10000 image size (8-bit), CPU processing time is found to be >250 ms, whereas the same for RTX 8000 is <20 ms indicating >12 times better performance. Likewise, RTX 8000 processing time for a 1000×1000-sized 8-bit image is

observed to be <300 μs, justifying a real-time applicability of the algorithm.

Fig. 8B shows a comparison of our processing-speed with a few state-of-the-art techniques: non-local mean denoising, morphological erosion, and morphological opening. For a fair comparison, each method is CUDA-accelerated with Quadro RTX 8000 while assessing the processing time. It is observed that, in comparison to non-local mean denoising, which is usually an expensive operation, our method works way faster.
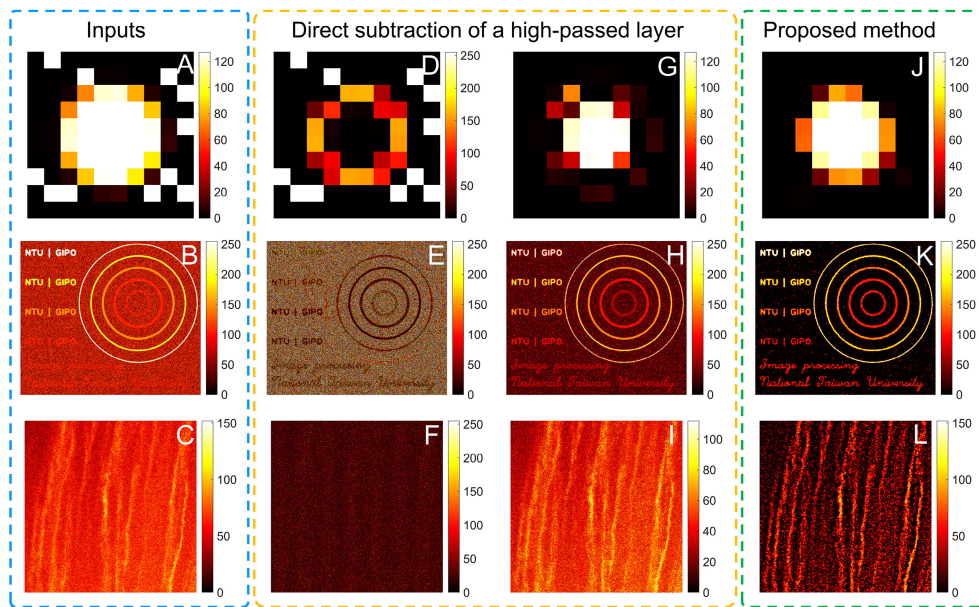
FIGURE 6. A comparison of *direct subtraction of a high-passed layer (from input)* with the *proposed algorithm*. (A)-(C) Noise-affected images, (D)-(F) Laplacian high-pass filtered layers of (A)-(C), respectively, (G)-(I) high-passed-layer subtracted results of (A)-(C), respectively, where, noisy background was well-suppressed in (G), but the same idea did not work satisfactorily in (H) & (I). (J)-(L) Results of the proposed algorithm for the same inputs in (A)-(C), respectively, showing an efficient suppression of noise in each case.

For instance, for a 10000×10000-sized 8-bit input, non-local mean denoising takes a duration of several seconds, whereas processing time for our method for the same input is ~19 ms. For the same input, a simple erosion operation takes ~7 ms, and an opening operation takes ~13 ms. Thus, a less than 20 ms processing time is observed for the proposed method and the morphological operations up-to an 8-bit input size of 10000×10000.

I. DISCUSSION

Contradicting a traditional UM approach, the proposed method does not involve addition of a high-passed image to the original input, and therefore does not result in a noise amplification. The sole purpose of our algorithm is to suppress high-frequency background noises in an image. The reported method does not demand any dedicated hardware to operate. We have demonstrated the effectiveness of the algorithm by means of both simulated and life-science imaging examples while securing a high processing speed via CUDA-acceleration.

For our algorithm to work best, it is expected that the noise-affected two-dimensional data set is digitized satisfying the respective Nyquist-Shannon sampling criterion [38], [39] in both dimensions, which will ensure at least 2×2 samples for the smallest recoverable structure. If undersampled, a single-sample information might be treated as a noise and thus might get eliminated or weakened. It is important that depending on the signal being digitized, the input-range of the digitizer should be set carefully to avoid saturation effect. Additionally, the input data should not go through

a conventional low-pass blurring filter prior to processing by our algorithm. A low-pass filter might distribute the high-frequency noise intensities to its darker-neighbors, and thereafter our algorithm might no longer be able to generate an effective subtraction-mask. It is important to note that, as a result of the second gaussian blur (BLUR2), the edges of the low-frequency structure in the MASK attain some non-zero values, which when subtracted from the INPUT, results in a suppression of the edges. To reduce this effect a smaller value of M is recommended. However, this effect might be helpful to improve the point spread function in some applications. To obtain the smooth layer of AMP1 we first performed a $3\times$ downscaling, and thereafter a 29×29-kernel gaussian blurring was applied. To produce a similar smoothness without the downscaling operation, we will require an even larger gaussian kernel which becomes expensive for a moderate to large-sized data set. However, a reduced smoothness of this layer might be still helpful in some applications to better-preserve useful high-frequency information. For an ultra-large data set (e.g., $> 10000 \times 10000$), a higher downscaling factor can be helpful so that the convolution remains computationally less expensive. However, an excessive downscaling might reduce the noise information and the resultant subtraction-mask might not remain effective enough. Alternatively, an ultra-large data set can be split into multiple blocks and can be processed in parallel taking advantage of CUDA-streaming. At the final stage, a bilinear interpolation can be applied to minimize any artifact arising at the joining of successive blocks. A disadvantage of GPU-processing is the additional time required for data downloading/ uploading to and from the host memory.
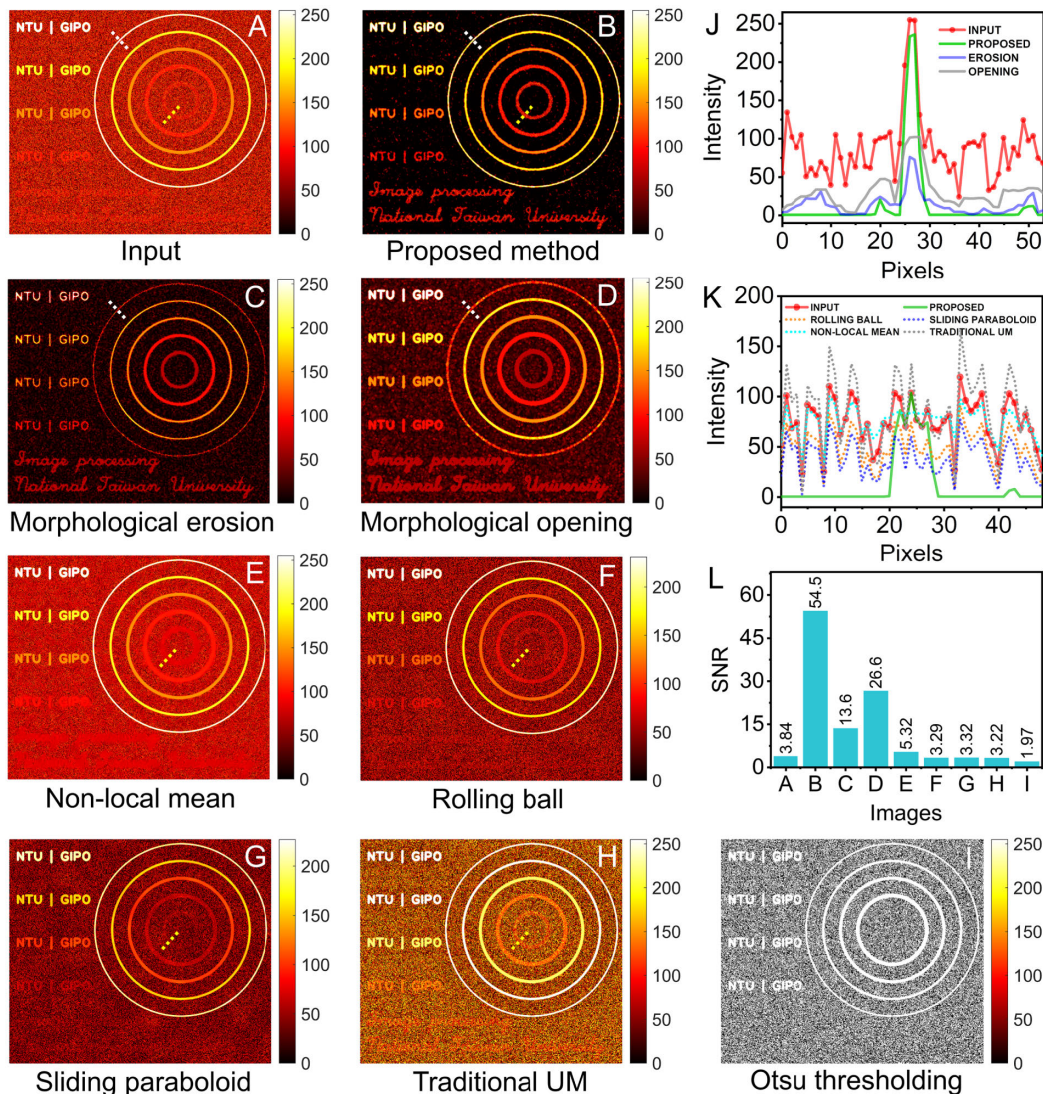
FIGURE 7. Comparison with a few existing techniques. (A) Noise-affected input image, (B) noise-suppressed output of the proposed algorithm, (C-I) output results of (C) morphological erosion, (D) morphological opening, (E) non-local mean denoising, (F-G) rolling ball & sliding paraboloid background subtraction, (H) traditional UM, and (I) Otsu thresholding, (J) intensity profiles along the white-dashed lines in (A)-(D), indicating that proposed algorithm (green curve) outperforms morphological operations (blue & gray curves) in context of suppressing noise while preserving useful information, (K) intensity profiles along the yellow-dashed lines in A-B, E-H, indicating that proposed algorithm (green curve) outperforms the counterparts in terms of noise suppression, (L) plot of SNRs for (A) 3.84, (B) 54.5, (C) 13.6, (D) 26.6, (E) 5.32, (F) 3.29, (G) 3.32, (H) 3.22, and (I) 1.97.

For a continuous data-processing application, an asynchronous transfer can be helpful to minimize this issue. As we have stated earlier, higher values of M and β are recommended if the INPUT is highly contaminated with noise. In such a case, the absolute intensities of the fine enough structures in the noise-suppressed output might tend to reduce slightly (refer to Figs. 2M-P), which can be of course improved with a normalization. Nevertheless, this effect should be taken into account in case of a quantitative analysis. Each example presented in this paper consists of a dark background and brighter signal. In case of a white background with darker signal, the 8-bit input and output data sets can be simply subtracted from 255 for our algorithm to work. Although we

have utilized 8-bit images in the examples, the algorithm can be also extended to a higher bit-depth data with appropriate gaussian kernels. Note that the reported technique is designed to suppress high-frequency background noises only, which is different from a background elimination process for foreground object segmentation [40]–[43] involved in various computer vision applications, such as, moving object detection in a video stream. If noise level is stronger than available signal, some informative samples belonging to low-frequency structures might get corrupted with noise, which our method cannot correct. Conventional denoising algorithms can be employed to our background-suppressed data to correct such corrupted samples.
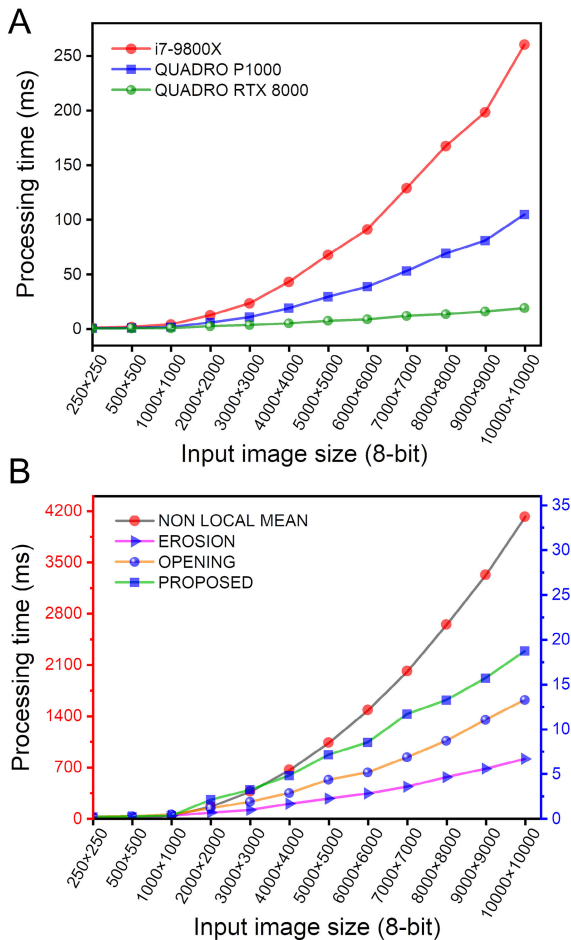
FIGURE 8. Assessment and comparison of processing speed. (A) Red, blue, and green curves represent processing time for our algorithm in milliseconds with respect to image size plotted for i7 9800X, Quadro P1000, and Quadro RTX 8000, respectively. Flat enough green curve shows a significant speed-improvement in comparison to the exponential red-curve. For a 10000 × 10000-sized 8-bit input, 9800X and RTX 8000-processing times are >250 ms and <20 ms, respectively, indicating a >12× performance boost via CUDA-acceleration, (B) gray, magenta, orange, and green curves depict the processing time in milliseconds with respect to image size plotted for non-local mean denoising, morphological erosion, morphological opening, and the proposed method, respectively. A less than 20 ms processing time is observed for the proposed method and the morphological operations up-to an input size of 10000 × 10000, whereas, non-local mean denoising requires up-to several seconds.

III. CONCLUSION AND FUTURE WORK

The reported method has a potential to be applied in various fields involving real-world data acquisition and analysis, such as, multi-modality microscopy, ultrasound/ computed tomography (CT)/ X-ray imaging, astronomical imaging, etc. In fluorescence microscopy, to reduce photobleaching and/or phototoxicity to an *in vivo* or *ex vivo* biological specimen, one has to excite the sample at a minimized average power which might lead to a poor SNR due to a strong noisy background. Apart from that, in case of volumetric imaging with an ultra-deep penetration, the emerging signal might get dominated by the background noise. In such situations, the proposed method can be helpful to recover the signal of interest.

While assessing the processing speed, we observe a less than 20 ms computation time (up-to a 10000 × 10000-sized 8-bit data set) for the proposed method, which is slower but mostly comparable to that of a morphological operation, and way faster than a computationally expensive algorithm, such as non-local mean denoising.

As of now, the effectiveness of the algorithm can be controlled with multiple parameters: α, β, and M. For user-friendly operations in a wide range of experimental conditions, it is thus worth extending the algorithm to be non-parametric where a real-time SNR measurement can be helpful to optimize the control parameters. Besides, instead of using a fixed global α, an independent layer of α-values can be chosen based on the signal strength to make the algorithm more effective particularly to be applied in a color image.

The algorithm when applied to a data-set, leaves the resolution least compromised. It can be therefore extended to a noise-compensated resolution-preserving local/global contrast optimization technique, which can be helpful to deal with the unwanted noise-amplification issue in a conventional contrast enhancing method.

DECLARATION OF INTERESTS
The reported technique is under a patent application process.

REFERENCES

[1] S. Vlassis, K. Doris, S. Siskos, and I. Pitas, "Analog implementation of erosion/dilation, median and order statistics filters," *Pattern Recognit.*, vol. 33, no. 6, pp. 1023–1032, Jun. 2000.

[2] S. Siskos, S. Vlassis, and I. Pitas, "Analog implementation of an order-statistics filter," *IEEE Trans. Circuits Syst. I, Fundam. Theory Appl.*, vol. 46, no. 10, pp. 1296–1300, Oct. 1999, doi: 10.1109/81.795845.

[3] A. Pullia and G. Ripamonti, "Minimum-noise filter for baseline estimation in radiation detection systems," *Nucl. Instrum. Methods Phys. Res. A, Accel. Spectrom. Detect. Assoc. Equip.*, vol. 376, no. 1, pp. 82–88, Jun. 1996, doi: 10.1016/0168-9002(96)00171-4.

[4] S. Siskos, S. Vlassis, and I. Pitas, "Analog implementation of fast min/max filtering," *IEEE Trans. Circuits Syst. II, Analog Digit. Signal Process.*, vol. 45, no. 7, pp. 913–918, Jul. 1998, doi: 10.1109/82.700945.

[5] E. S. Gedraite and M. Hadad, "Investigation on the effect of a Gaussian Blur in image filtering and segmentation," in *Proc. ELMAR*, Sep. 2011, pp. 393–396.

[6] U. Erkan, D. N. H. Thanh, L. M. Hieu, and S. Enginoglu, "An iterative mean filter for image denoising," *IEEE Access*, vol. 7, pp. 167847–167859, 2019, doi: 10.1109/ACCESS.2019.2953924.

[7] M. Elad, "On the origin of the bilateral filter and ways to improve it," *IEEE Trans. Image Process.*, vol. 11, no. 10, pp. 1141–1151, Oct. 2002, doi: 10.1109/TIP.2002.801126.

[8] P. M. Narendra, "A separable median filter for image noise smoothing," *IEEE Trans. Pattern Anal. Mach. Intell.*, vol. PAMI-3, no. 1, pp. 20–29, Jan. 1981, doi: 10.1109/TPAMI.1981.4767047.

[9] F. M. Bayer, A. J. Kozakevicius, and R. J. Cintra, "An iterative wavelet threshold for signal denoising," *Signal Process.*, vol. 162, pp. 10–20, Sep. 2019, doi: 10.1016/j.sigpro.2019.04.005.

[10] J. Chen, J. Benesty, Y. Huang, and S. Doclo, "New insights into the noise reduction Wiener filter," *IEEE Trans. Audio, Speech, Language Process.*, vol. 14, no. 4, pp. 1218–1234, Jul. 2006, doi: 10.1109/TSA.2005.860851.

[11] S. S. S. Poon, J. T. Wong, D. N. Saunders, Q. C. Ma, S. McKinney, J. Fee, and S. A. J. R. Aparicio, "Intensity calibration and automated cell cycle gating for high-throughput image-based siRNA screens of mammalian cells," *Cytometry A*, vol. 73A, no. 10, pp. 904–917, Oct. 2008, doi: 10.1002/cyto.a.20624.

[12] T. Q. Syed, V. Vigneron, S. Lelandais, G. Barlovatz-Meimon, M. Malo, C. Charriere-Bertrand, and C. Montagne, "Detection and counting of *in vivo* cells to predict cell migratory potential," in *1st Workshops Image Process. Theory, Tools Appl.*, Sousse, Tunisia, pp. 1–8, doi: 10.1109/IPTA.2008.4743748.

[13] G. Selvaggio, F. Ceroni, E. Giordano, and J. V. Lorenzo-Ginori, "Evaluation of the expression level of a fluorescent protein in single cells through digital image processing," in *Proc. IFMBE*, F. J. Méndez, Eds., vol. 33, 2013, pp. 1007–1010, doi: 10.1007/978-3-642-21198-0_256.

[14] L. R. Sysko and M. A. Davis, "From image to data using common image-processing techniques," *Current Protocols Cytometry*, vol. 54, no. 1, p. 12, Oct. 2010, doi: 10.1002/0471142956.cy1221s54.

[15] L. Möckl, A. R. Roy, P. N. Petrov, and W. E. Moerner, "Accurate and rapid background estimation in single-molecule localization microscopy using the deep neural network BGnet," *Proc. Nat. Acad. Sci. USA*, vol. 117, no. 1, pp. 60–67, Jan. 2020, doi: 10.1073/pnas.1916219117.

[16] S. R. Sternberg, "Biomedical image processing," *Computer*, vol. 16, no. 1, pp. 22–34, Jan. 1983, doi: 10.1109/MC.1983.1654163.

[17] J. C. Russ, "Acquiring images," in *The Image Processing Handbook*. Boca Raton, FL, USA: CRC Press, 2006, pp. 28–29.

[18] K. Kaur, N. Jindal, and K. Singh, "Fractional derivative based unsharp masking approach for enhancement of digital images," *Multimedia Tools Appl.*, vol. 80, no. 3, pp. 3645–3679, Jan. 2021, doi: 10.1007/s11042-020-09795-5.

[19] J. Joseph, B. N. Anoop, and J. Williams, "A modified unsharp masking with adaptive threshold and objectively defined amount based on saturation constraints," *Multimedia Tools Appl.*, vol. 78, no. 8, pp. 11073–11089, Apr. 2019, doi: 10.1007/s11042-018-6682-1.

[20] S. Kansal, S. Purwar, and R. K. Tripathi, "Image contrast enhancement using unsharp masking and histogram equalization," *Multimedia Tools Appl.*, vol. 77, no. 20, pp. 26919–26938, Mar. 2018, doi: 10.1007/s11042-018-5894-8.

[21] W. Ye and K.-K. Ma, "Blurriness-guided unsharp masking," *IEEE Trans. Image Process.*, vol. 27, no. 9, pp. 4465–4477, Sep. 2018, doi: 10.1109/TIP.2018.2838660.

[22] A. Polesel, G. Ramponi, and V. J. Mathews, "Image enhancement via adaptive unsharp masking," *IEEE Trans. Image Process.*, vol. 9, no. 3, pp. 505–510, Mar. 2000, doi: 10.1109/83.826787.

[23] S. C. F. Lin, C. Y. Wong, G. Jiang, M. A. Rahman, T. R. Ren, N. Kwok, H. Shi, Y.-H. Yu, and T. Wu, "Intensity and edge based adaptive unsharp masking filter for color image enhancement," *Optik*, vol. 127, no. 1, pp. 407–414, 2016, doi: 10.1016/j.ijleo.2015.08.046.

[24] S. Chiandussi and G. Ramponi, "Nonlinear Unsharp Masking for the enhancement of document images," in *Proc. EUSIPCO*, 1996, pp. 1–4.

[25] G. Scognamiglio, G. Ramponi, A. Rizzi, and L. Albani, "A rational unsharp masking method for TV applications," in *Proc. Int. Conf. Image Process.*, 1999, pp. 247–251, doi: 10.1109/ICIP.1999.819588.

[26] M. E. Couwenhoven, R. A. Senn, and D. H. Foos, "Enhancement method that provides direct and independent control of fundamental attributes of image quality for radiographic imagery," *Proc. SPIE Med. Imag.*, vol. 5367, pp. 474–481, May 2004, doi: 10.1117/12.537272.

[27] R. M. Lapp, Y. Kyriakou, M. Kachelrieß, S. Wilharm, and W. A. Kalender, "Interactively variable isotropic resolution in computed tomography," *Phys. Med. Biol.*, vol. 53, no. 10, pp. 2693–2713, Apr. 2008, doi: 10.1088/0031-9155/53/10/017.

[28] X. Duan, Y. Mei, S. Wu, Q. Ling, G. Qin, J. Ma, C. Chen, H. Qi, L. Zhou, and Y. Xu, "A multiscale contrast enhancement for mammogram using dynamic unsharp masking in Laplacian pyramid," *IEEE Trans. Radiat. Plasma Med. Sci.*, vol. 3, no. 5, pp. 557–564, Sep. 2019, doi: 10.1109/TRPMS.2018.2876873.

[29] Siddharth, R. Gupta, and V. Bhateja, "A log-ratio based unsharp masking (UM) approach for enhancement of digital mammograms," in *Proc. CUBE Int. Inf. Technol. Conf.*, 2012, pp. 26–31, doi: 10.1145/2381716.2381723.

[30] B. N. Anoop, J. Joseph, J. Williams, J. S. Jayaraman, A. M. Sebastian, and P. Sihota, "A prospective case study of high boost, high frequency emphasis and two-way diffusion filters on MR images of glioblastoma multiforme," *Australas. Phys. Eng. Sci. Med.*, vol. 41, no. 2, pp. 415–427, Apr. 2018, doi: 10.1007/s13246-018-0638-7.

[31] Siddhartha and V. Bhateja, "A modified unsharp masking algorithm based on region segmentation for digital mammography," in *Proc. 4th Int. Conf. Electron. Comput. Technol. (ICECT)*, vol. 1, Apr. 2012, pp. 63–67.

[32] W. Denk, J. H. Strickler, and W. W. Webb, "Two-photon laser scanning fluorescence microscopy," *Science*, vol. 248, no. 4951, pp. 73–76, Apr. 1990, doi: 10.1126/science.2321027.

[33] P. C. Cheng, C. K. Sun, B. L. Lin, F. J. Kao, and S. W. Chu, "Biological multi-modality nonlinear spectromicroscopy: Multiphoton fluorescence, second- and third-harmonic generation," *Scanning*, vol. 23, no. 2, pp. 109–110, 2001.

[34] C. Huang and Y. Zhu, "New morphological filtering algorithm for image noise reduction," in *Proc. 2nd Int. Congr. Image Signal Process.*, Tianjin, China, 2009, pp. 1–6, Oct. 2009, doi: 10.1109/CISP.2009.5303495.

[35] A. Buades, B. Coll, and J.-M. Morel, "Nonlocal image and movie denoising," *Int. J. Comput. Vis.*, vol. 76, no. 2, pp. 123–139, Jul. 2007, doi: 10.1007/s11263-007-0052-1.

[36] J. B. Kelley and B. M. Paschal, "Fluorescence-based quantification of nucleocytoplasmic transport," *Methods*, vol. 157, pp. 106–114, Mar. 2019, doi: 10.1016/j.ymeth.2018.11.002.

[37] N. Otsu, "A threshold selection method from gray-level histograms," *IEEE Trans. Syst., Man, Cybern.*, vol. 9, no. 1, pp. 62–66, Jan. 1979, doi: 10.1109/TSMC.1979.4310076.

[38] C. E. Shannon, "Communications in the presence of noise," *Proc. IRE*, vol. 37, no. 1, pp. 10–21, Jan. 1949.

[39] H. Nyquist, "Certain topics in telegraph transmission theory," *Trans. Amer. Inst. Electr. Engineers*, vol. 47, no. 2, pp. 617–644, Apr. 1928, doi: 10.1109/T-AIEE.1928.5055024.

[40] T. Bouwmans, "Traditional and recent approaches in background modeling for foreground detection: An overview," *Comput. Sci. Rev.*, vol. 11, pp. 31–66, May 2014, doi: 10.1016/j.cosrev.2014.04.001.

[41] A. Sobral and A. Vacavant, "A comprehensive review of background subtraction algorithms evaluated with synthetic and real videos," *Comput. Vis. Image Understand.*, vol. 122, pp. 4–21, May 2014, doi: 10.1016/j.cviu.2013.12.005.

[42] Y. Benezeth, P.-M. Jodoin, B. Emile, H. Laurent, and C. Rosenberger, "Comparative study of background subtraction algorithms," *J. Elec. Imag.*, vol. 19, pp. 1–12, Jul. 2010, doi: 10.1117/1.3456695.

[43] W. Kim and C. Jung, "Illumination-invariant background subtraction: Comparative review, models, and prospects," *IEEE Access*, vol. 5, pp. 8369–8384, 2017, doi: 10.1109/ACCESS.2017.2699227.

BHASKAR JYOTI BORAH was born in Assam, India, in January 1995. He received the master's degree from Tezpur University, Assam, in 2017. He is currently pursuing the Ph.D. degree with the Graduate Institute of Photonics and Optoelectronics, National Taiwan University (NTU), Taipei, Taiwan.

His focus of research in NTU is towards the development of novel technologies for the advancement of nonlinear optical microscopy. One of his inventions titled "A large-angle optical raster scanning system for deep tissue imaging" has recently been granted with a patent in Taiwan. He was awarded with the Gold Medal in the discipline of physics (five-year Integrated M.Sc., 2012–2017) by Tezpur University. He was awarded with the Inspire Fellowship (2012–2017) instituted by the Department of Science and Technology, India; the G. N. Ramachandran Fellowship for young promising researchers (2016) instituted by Alumni of IIT Madras, India; and the Taiwan Scholarship (2017–2021) by the Ministry of Education, Taiwan.

CHI-KUANG SUN (Fellow, IEEE) received the Ph.D. degree in applied physics from Harvard University, in 1995.

He was an Assistant Researcher with the UCSB QUEST Center, from 1995 to 1996. He joined the National Taiwan University (NTU) Faculty, in 1996, where he is currently the Life Distinguished Professor of electrical engineering and photonics. He has served as the Chairman of the Photonics Program, Ministry of Science and Technology, Taiwan. He is also the Founder and the Chief Investigator of the Molecular Imaging Center, one of the university-level excellence centers at NTU. He was the Deputy Dean of the EECS College, NTU. His research interests include optical molecular imaging, nonlinear microscopy, ultrafast phenomena, nano-ultrasonics, THz health care, advanced femtosecond laser technologies, and applications in virtual biopsy diagnosis, treatment and therapy assessment, surgical guidance, neural science, virus epidemic control, paleontology, interfacial water imaging, and boson peak studies. He is a Fellow of OSA and SPIE.

● ● ●